Grain growth behaviour during near-γ' solvus thermal exposures in a polycrystalline nickel-base superalloy

D.M. Collins, B.D. Conduit, H.J. Stone,
M.C. Hardy, G.J. Conduit & R.J. Mitchell

Grain growth behaviour during near γ' solvus thermal exposures in a polycrystalline nickel-base superalloy

D.M. Collins[a], B.D. Conduit[b], H.J. Stone[c], M.C. Hardy[d], G.J. Conduit[e], R.J. Mitchell[f]

[a]*Department of Materials, University of Oxford, Oxford, OX1 3PH, UK*
[b]*Strategic Research Centre, Rolls-Royce plc, Sinfin-A, PO BOX 31, DE24 8BJ, UK*
[c]*Rolls-Royce UTC, Department of Materials Science & Metallurgy, University of Cambridge, Pembroke Street, Cambridge CB2 3QZ, UK*
[d]*Rolls-Royce plc., ELT-10, PO BOX 31, Derby, DE24 8BJ, UK*
[e]*Theory of Condensed Matter Group, Department of Physics, Cavendish Laboratory, 19 J.J. Thomson Avenue, Cambridge CB3 0HE, UK*
[f]*Rolls-Royce plc., Raynesway, PO BOX 2000, Derby, DE21 7XX, UK*

Abstract

The grain growth behaviour that occurs during near solvus isothermal and transient heat treatments and the influence of primary γ' has been studied in the advanced polycrystalline nickel-base superalloy, RR1000. Experimental observations showed grain growth can be related to $\bar{D}_{\text{lim}}$, a theoretical grain size limit that accounts for the time dependent pinning contribution from the full primary γ' precipitate size distribution. This term was also used to describe the pinning contribution from MC-carbides, which limits grain size in the absence of primary γ'. The values of $\bar{D}_{\text{lim}}$ were calculated using both experimental data and simulated data obtained from the software, *PrecipiCalc*. The grain growth model proposed by Andersen & Grong [1] was modified to incorporate the pinning effect of primary γ' and MC-carbides. This was used to predict the grain sizes for a range of heat treatment times, incorporating the calculated $\bar{D}_{\text{lim}}$ values. Material dependent grain growth coefficients were simultaneously fitted by minimising the difference between the simulated and experimental grain sizes. Good correlation was achieved between the modelled and experimental grain sizes, though agreement was superior with *PrecipiCalc* data. This was attributed to the removal of experimental scatter, found to be important when using this method.

Key words: grain growth, precipitation, coarsening, heat treatment

1. Introduction

The demanding service conditions in the hottest stages of gas turbine engines are almost exclusively served by components fabricated from nickel-based superalloys. At elevated temperatures, this important classification of materials have exceptional mechanical properties [2]. This performance can largely be attributed to its microstructure, which in its simplest form consists of a γ, A1 matrix with a dispersion of coherent γ', $L1_2$ precipitates. In the latest, powder processed turbine discs, the nickel-base superalloy will typically exhibit a trimodal γ' precipitate distribution. During processing, the material will be consolidated by hot isostatic pressing (HIP), allowing primary γ' to form. Subsequent subsolvus extrusion and forging affect the volume fraction and precipitate size, which will typically be between 1 µm and 5 µm. The primary γ' has the role of restricting grain boundary migration during subsolvus solution heat treatments. Subsequent heat treatments can be used to promote the formation of two further intragranular precipitate populations, denoted as secondary γ' and tertiary γ', with diameters typically between 100 & 400 nm and 5 & 50 nm respectively are also formed [3]. The lattice parameters of the γ and γ' phases are tailored to give a low lattice misfit, particularly at service temperatures, thereby reducing deterioration of mechanical properties due to precipitate coarsening or morphological changes [4].

The mechanical properties of nickel-base superalloys are largely governed by the interaction between the precipitates and weakly or strongly coupled dislocations. These properties are therefore critically controlled by the size, distribution and morphology of the γ' precipitates [4, 5]. It is generally considered desirable to heat treat the alloy to have as many γ' precipitates as possible within the diameter range which is most beneficial to the mechanical properties [6, 7]. As the primary γ' precipitates are too large to contribute to the static strength of the material, the volume fraction of the primary γ' should therefore be reduced. However, a minimum volume fraction of γ' must remain present to resist grain boundary migration and hence preserve a sufficiently fine grain size.

Historically, the grain size in a turbine disc was selected to be a compromise between the varying property requirements at different radial locations across the disc [6]. At the rim of the disc, high temperatures and moderate stresses demand good creep performance and resistance to dwell crack growth, both of which improve with an increased grain size. Whilst in the bore of the disc, lower temperatures and higher stresses demand a fine grain microstructure to deliver good tensile and low cycle fatigue properties [8]. The contemporary process of dual microstructure heat treatments (DMHT) enables an appropriate grain size to be produced for each radial location, thereby offering improved performance over the turbine disc manufacturing

processes historically used.

A dual microstructure is achieved by subjecting the disc forging to location specific heat treatments. Of the large gas turbine manufacturers, each has developed a unique process to provide these heat treatments, controlling the manner in which heat is delivered and extracted from the component [9, 10, 11]. Common to all, however, is a subsolvus heat treatment close to the disc bore, retaining the trimodal γ' distribution, whereas the rim is subjected to a supersolvus heat treatment, dissolving the primary γ' and thus permitting grain coarsening.

The advanced polycrystalline nickel-base superalloy, RR1000 [12], is a candidate material for DMHT [11, 3], and in the present study, the grain growth response is examined for the near-γ' solvus heat treatments required for the optimisation of such a process. This study includes both isothermal and transient heat treatments, representative of the range of conditions used during component manufacture. This is subdivided into (1) experimental observations of grain size, primary γ' and carbide precipitate size distributions (PSDs), and (2) the simulation of grain size using a grain growth model. Comparisons are also made between the precipitate pinning effects from experimentally measured PSDs, and PSDs predicted using the commercial modelling software *PrecipiCalc*.

2. Background

For a single phase alloy of mean grain diameter, $\bar{D}$, grain growth will be dependent on the mobility of a grain boundary and the driving force, which is proportional to $2\sigma/\bar{D}$, where σ is the surface energy per unit area. Empirically, the grain growth may be described by the following relation [13]:

$$\bar{D} = k_1 t^n \tag{1}$$

where k_1 is a constant with respect to the system temperature, t is time and n is a grain growth exponent. The value of n has been discussed by Fullman *et al.* [14], who showed that a value of 0.5 will only be reached in very pure metals and at temperatures close to the melting point. In Equation 1, the starting mean grain diameter at $t = 0$, is assumed to be equal to zero, and hence this relation is only suitable for long annealing times where the starting grain diameter may be neglected. For materials operating in a regime of normal grain growth under isothermal conditions, Hu and Rath [14] described the grain size by

$$\bar{D}^{\frac{1}{n}} - \bar{D}_0^{\frac{1}{n}} = k_2 \exp\left(\frac{-Q_{\text{app}}}{\mathcal{R}T}\right) t \tag{2}$$

where k_2 is a constant dependent on the physical kinetics, $\bar{D}_0$ is an initial mean grain size, Q_{app} is the apparent grain boundary activation energy, $\mathcal{R}$ is the molar gas constant, t is the annealing time and T is temperature. In this example, n is expected to be between 0.1 and 0.5, depending on the resistive force to grain boundary migration from solute atoms [15]. The driving force for growth can be attributed to an average thermodynamic driving pressure of a curved grain boundary, P_{g}, with an associated grain boundary interfacial energy, σ_{gb}. This relationship is given as

$$P_{\text{g}} = k_3 \left(\frac{\sigma_{\text{gb}}}{\bar{D}}\right) \tag{3}$$

where k_3 is a constant dependent on the system characteristics.

Grain growth can be hindered by a distribution of second phase particles, as first reported by Zener [16]. For the application to nickel-base superalloys, Song *et al.* [17] observed the Zener pinning effect on the growth of γ from both γ' and other inert particles, such as yttrium oxides or MC-carbides (M denotes a metallic element). The particle/precipitate sizes and volume fractions of the phases were additionally found to be highly important. The powder process used during turbine disc manufacture has been observed to influence the grain growth behaviour. In the process of solidification, following gas atomisation, certain elements segregate to the surface of the powder particles. These tend to be carbide formers, such as Ti, Ta, Nb and Hf. Surfaces of the powder particles also tend to pick up oxygen and nitrogen from atomisation, screening and blending despite the use of a high vacuum or an inert atmosphere. During hot isostatic pressing, carbon diffuses to the surface of the particles and reacts with surface species to form oxy-carbides. These decorate the prior particle boundaries (PPBs) and heavily influence the grain size and morphology following the HIP process. In addition, alloy RR1000 contains very small HfO_2 particles, which also provide a contribution to grain boundary pinning [18]. Opposing the driving pressure for grain growth is the Zener drag pressure, denoted as P_{z}, which is a function of the precipitate volume fraction, ϕ, and the particle radius, r, giving

$$P_{\text{z}} = k_4 \sigma_{\text{gb}} \left(\frac{\phi}{r}\right) \tag{4}$$

The constant, k_4, is a system dependent coefficient. The relationship between the thermodynamic driving pressure and the Zener drag has been used by Hu and Rath [14], to describe the velocity of the migrating boundary, v,

$$v = M\left(P_{\text{g}} - P_{\text{z}}\right)^{\frac{1}{n}-1} \tag{5}$$

where M is the mobility of the grain boundary. The driving force per unit volume of boundary is simply the difference between the thermodynamic driving pressure, P_{g}, and the resistive pressure due to Zener drag, P_{z}. When $n = 0.5$, the grain boundary velocity varies linearly with the driving pressure. When $n < 0.5$, the grain boundary velocity varies with a power of the driving pressure [14].

Modelling of grain growth in nickel-base superalloys with the inclusion of pinning effects using phase field methods can also be performed, e.g. [19]. Whilst such models have the potential to include all of the governing physics, they arguably remain unattractive, particularly for commercial applications due to the requirement of significant computational power, the number of assumptions made and the need for considerable thermophysical data. One alternative may be to use a mean-field statistical method for grain growth, which again may incorporate a static or non-static pinning effect [20].

An analytical model which describes grain growth behaviour in the presence of precipitates that are allowed to grow or dissolve as the grains are simultaneously growing has been developed by Andersen & Grong[1]. This model permits experimental linear intercept measurements of mean grain size, denoted as

$\bar{D}^*$, to be converted to equivalent 3D measurements, and uses these to predict the 3D grain growth behaviour for an arbitrary thermal cycle. Therefore, from experimentally determined 2D mean grain diameters, a conversion of $\bar{D} = \frac{3}{2}\bar{D}^*$ is used, assuming a log-normal grain size distribution [14, 1].

This model has been successfully used to describe normal [1] or abnormal grain growth [21], and has been applied to a number of different metallurgical systems i.e. [22, 23, 24]. Following the model for normal grain growth, given in Equations 3 & 4, the velocity, v, and mobility, M, are described by the following expressions; $v = \frac{1}{2}(\mathrm{d}\bar{D}/\mathrm{d}t)$ and $M = M_0 \exp(-Q_{\mathrm{app}}/\mathcal{R}T)$ [14] and substituted into Equation 5 to give a generic grain growth model which accounts for the presence of impurities and pinning second phase particles. M_0 is a kinetic constant in the mobility. In this way, the rate of change of grain size is given by

$$\frac{\mathrm{d}\bar{D}}{\mathrm{d}t} = 2M_0(k_3\sigma_{\mathrm{gb}})^{1/n-1} \exp\left(\frac{-Q_{\mathrm{app}}}{\mathcal{R}T}\right)\left[\frac{1}{\bar{D}} - \frac{k_4\phi}{k_3 r}\right]^{\frac{1}{n}-1} \tag{6}$$

This differential equation can be integrated to evaluate the grain size as a function of time. It is therefore possible to include a dynamic process such as precipitation, incorporating the temporal evolution of volume fraction and particle radius. With this approach, grain growth can be evaluated in systems of stable, growing or dissolving precipitates. Many of the constants can be collapsed into simpler forms, specifically,

$$M_0^* = 2M_0\left(k_3\sigma_{\mathrm{gb}}\right)^{\frac{1}{n}-1} \tag{7}$$

$$k = \frac{k_3}{k_4} \tag{8}$$

where M_0^* and k are both constants based on physical parameters. The value of k was given as $4/3$ by Zener, though this value has been disputed and recalculated numerous times with limited agreement, as summaried by ref. [25], showing a dependence on the assumptions used to model the drag force [15]. By agglomerating the constants in this way, Equation 6 can be simplified to give

$$\frac{\mathrm{d}\bar{D}}{\mathrm{d}t} = M_0^* \exp\left(\frac{-Q_{\mathrm{app}}}{\mathcal{R}T}\right)\left[\frac{1}{\bar{D}} - \frac{1}{k}\frac{\phi}{r}\right]^{\frac{1}{n}-1} \tag{9}$$

The limiting grain size, $\bar{D}_{\mathrm{lim}}$, is therefore related the radius and volume fraction of the pinning precipitates, as well as the Zener coefficient, by

$$\bar{D}_{\mathrm{lim}} = k\left(\frac{r}{\phi}\right). \tag{10}$$

Practically, grains will be allowed to grow as the volume fraction of pinning precipitates decreases or their radius increases. Equation 9 can be rearranged and solved as definite integrals for $\bar{D}$ and t as follows,

$$\int_{D_0}^{\bar{D}_t} \frac{\mathrm{d}\bar{D}}{\left(\frac{1}{\bar{D}} - \frac{1}{\bar{D}_{\mathrm{lim}}}\right)^{\frac{1}{n}-1}} = \int_{t_1}^{t_2} M_0^* \exp\left(\frac{-Q_{\mathrm{app}}}{\mathcal{R}T}\right)\mathrm{d}t. \tag{11}$$

For the condition of $n = 0.5$, Equation 11 can be solved for $\bar{D}$ analytically. For $n \neq 0.5$, the integral has to be solved using a numerical method.

3. Experimental details

In this investigation, the relationship between grain size, and the size distribution of the primary γ' and carbides of the polycrystalline nickel-base superalloy, RR1000, were investigated as a function of heat treatment conditions. The starting microstructure of the material was dictated by the prior thermo-mechanical deformation, having been HIPed and extruded in a subsolvus condition. This billet material was sectioned into cubes measuring $5 \times 5 \times 5$ mm and subjected to the matrix of heat treatments listed below.

1. *Isothermal heat treatments*
   Samples were heat treated for 2, 4, 6, 8, 10, 20, 30, 40, 60, 90 and 120 minutes at temperatures between 1120°C and 1200°C in 10°C intervals.
2. *Transient heat treatments*
   Samples were subjected to varying thermal cycles with a monotonic heating rate of 222°C h^{-1}. This rate was selected to closely represent a typical thermal cycle experienced by a turbine disc during a processing heat treatment. Samples were heated from 3 starting temperatures: 1038°C, 1052°C and 1066°C. The heat treatments were interrupted when selected temperatures had been reached, ranging from 1090°C to 1200°C in 10°C intervals.

For all of the samples, after they were inserted into the furnace, the temperature initially dropped. As a result, the heat treatment time was started once the furnace temperature had returned to the target temperature. This was consistently observed to be less than one minute.

Each heat treated sample was mounted, ground and polished to a 1 µm finish. The samples were then electrolytically etched at ~4 V using an aqueous solution of 10 vol.% phosphoric acid, leaving the γ' precipitates in relief from the γ surface enabling microstructural imaging using optical and electron microscopy.

A number of microstructural features present in RR1000 that are considered in this study are shown in Figure 1. The optical micrograph, (a), shows a supersolvus microstructure where only γ grain boundaries can be observed at this magnification. A backscattered SEM micrograph, (b), shows the fine grain structure of a sample having received a subsolvus heat treatment, with primary γ' present at the grain boundaries. A higher magnification TEM image, (c) prepared using a carbon replica method [26], shows the intragranular secondary and tertiary γ'. A high voltage backscattered electron image is shown in (d), and reveals the distribution of carbides present in the material. Whilst observation of primary γ' was possible using optical microscopy, large discrepancies were found with precipitate sizes obtained using SEM. The etching process leaves the γ' in relief and presents a problem when using optical microscopy as the raised features glare when observed, resulting in their volume fractions and precipitate sizes being overestimated. The reliable characterisation of the size, distribution, morphology and volume fraction of γ', can therefore only be achieved with electron microscopy. Optical microscopy was therefore used for grain size assessment only, as these measurements were not compromised by this phenomenon.

Mean 2D grain sizes were obtained using the linear intercept method [27] for each material condition. Backscattered electron micrographs were captured using a JEOL 6340F FEG-SEM at the same magnification. Images were taken at a series of random locations throughout each sample, for at least 200 precipitates to be measured. The primary γ' size distributions were obtained from the raw images using the image analysis software, *ImageJ* [28, 29]. During image processing, the primary γ' precipitates were manually isolated by selecting regions of the micrograph that exceeded a greyscale threshold. These selected isolated regions were next converted to binary images and individually measured. The measured area of each precipitate was then converted to an equivalent radius, assuming the precipitate was spherical. The total area fraction occupied by the precipitates was used to provide an equivalent measurement of the volume fraction [30].

4. Experimental Results

4.1. Material Starting Condition

The material characterised in this study had an initial grain size of 3.0 µm ± 0.2 µm, where the error is given as one standard deviation. The particle sizes of the primary γ' are presented in Figure 2 (a) along with a log-normal size distribution fitted to the data. The precipitates identified as primary γ' were observed to be present on the grain boundaries and at triple points, showing quite irregular, globular morphology. The volume fraction of primary γ' in this starting conditions was found to be 0.17 ± 0.01, with a mean precipitate radius of 0.39 µm ± 0.01 µm.

4.2. Pinning from Carbides

Microstructural analyses were also conducted to characterise the carbides present. Backscattered electron imaging was performed using a CamScan MX2600 SEM at an applied voltage of 30 keV. An example micrograph is shown in Figure 1 (d). Measurement of these carbides gave a volume fraction of 0.0022 ± 0.0011 and a mean particle diameter of 140 ± 34 nm. An example size distribution from these carbides is shown in Figure 2 (b). Equilibrium thermodynamic calculations at the heat treatment temperature using *JMatPro* [31] predicted MC carbides are the only stable carbides at heat treatment temperatures in the vicinity of the γ' solvus temperature. The MC carbides are predicted to be present with a volume fraction of 0.0018 at 1100°C; and, that this volume fraction remains approximately constant between ~960°C and ~1260°C. This is in good agreement with the experimental measurements made in this study, and with other results reported in prior investigations on RR1000 for a range of heat treatments [32]. Additionally, the measured carbide particle size distributions did not noticeably change within the matrix of heat treatment conditions studied.

4.3. Isothermal Heat Treatments

The measured grain sizes obtained following the isothermal heat treatments are presented in Figure 3 (a). These results will be discussed with reference to the corresponding primary γ' volume fractions, shown in Figure 6 (a). With a starting 2D

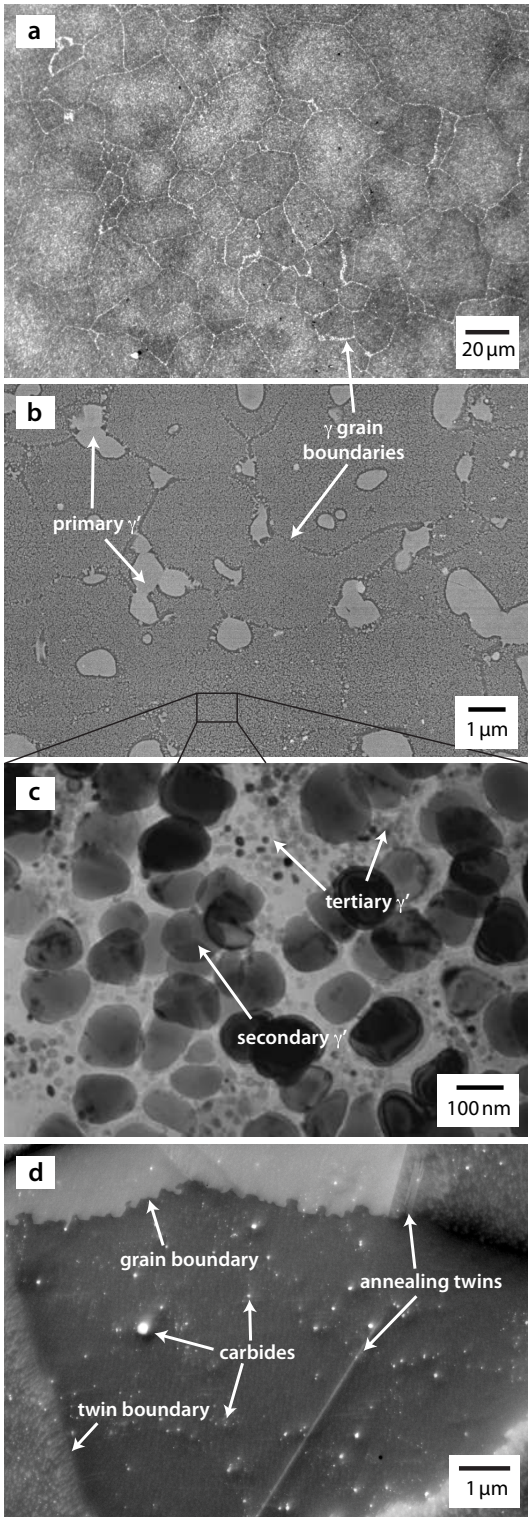

Figure 1: Example optical micrographs of RR1000 heat treated in the conditions (a) supersolvus, 1170°C for 40 minutes, and (b) subsolvus, 1140°C for 40 minutes. Smaller intragranular secondary and tertiary γ distributions are observed at higher magnification using TEM. Carbon replicas were used to produce the micrograph shown in (c). Identification of carbides and other microstructural features in RR1000 from backscattered SEM image at 30 keV shown in (d).

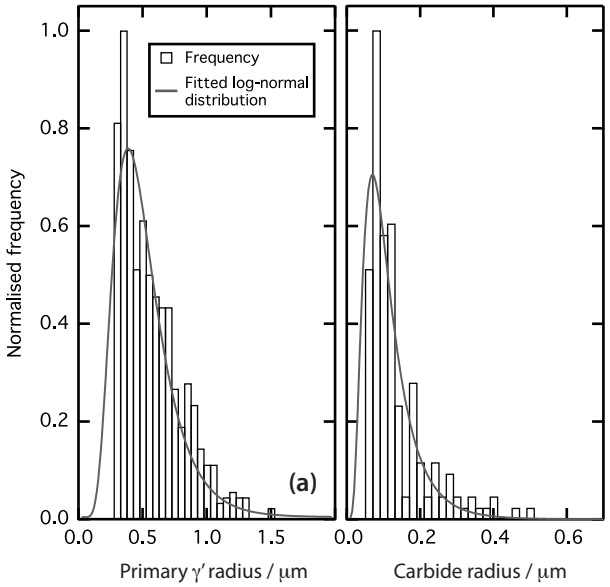

Figure 2: Particle size distributions for (a) primary γ' precipitates from the starting, billet condition, and (b), carbides particles, measured from material subjected to an isothermal heat treatment of 2 minutes at 1200°C. These distributions have been fitted with a log-normal function.

mean grain diameter of 3.0 μm at 1120°C, the growth is restricted by pinning primary γ' and does not exceed 3.8 μm after 120 minutes at this temperature. During this period, the γ' volume fraction is initially 0.17 and drops to ~0.09. After this time at 1120°C, it is expected that the volume fraction will have approached equilibrium. At the higher temperature of 1130°C, the γ' dissolution is increased, with the volume fraction reducing to 0.09 in just 6 minutes. After 120 minutes at 1130°C, the volume fraction drops to approximately 0.04, allowing steady, but limited, grain growth up to an observed mean grain diameter of ~5 μm.

Rapid grain growth occurs at temperatures of 1140°C and above. At 1140°C, the γ' volume fraction drops to 0.04 within 8 minutes, and falls further to approximately 0.02 after 120 minutes. Though primary γ' remains present, it appears that the pinning effect of the precipitates has been reduced enough to no longer effectively resist the migrating grain boundaries. After all of the primary γ' has dissolved, the rate of grain growth shows comparatively small increases with increasing temperature. This suggests that the grain size is now limited by the pinning from a different particle distribution once a certain grain size is reached. It is proposed that the presence of carbides of sufficient size and volume fraction may account for the observed retardation of grain growth at these temperatures. Evidence of inert particles including MC carbide pinning has also been reported in other Ni-base superalloys [33, 17]. However, the lower volume fraction and finer size of the carbides, means they do not affect the grain growth behaviour when the grains are fine, instead the pinning effect is dominated by primary γ' and will therefore be controlled by the r/ϕ ratio of these phases, as expressed in Equation 10. At temperatures of 1150°C and above, complete γ' dissolution is expected, as shown by a differ-

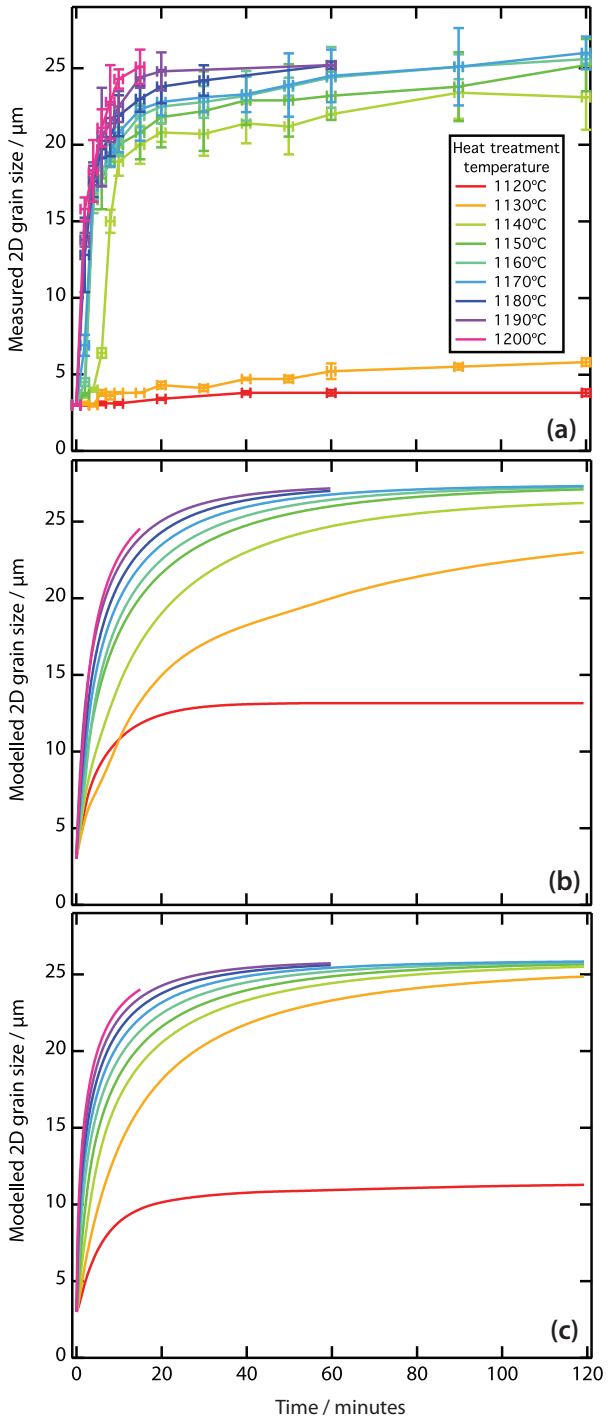

Figure 3: Grain size as a function of time at various isothermal heat treatment temperatures. Experimental observations are shown in (a). In (b), modelled grain growth results are shown using $\bar{D}_{\text{lim}}/k$ values from measurements, and (c), $\bar{D}_{\text{lim}}/k$ values are calculated from *PrecipiCalc* simulations. Both models shown had all data fitted simultaneously.

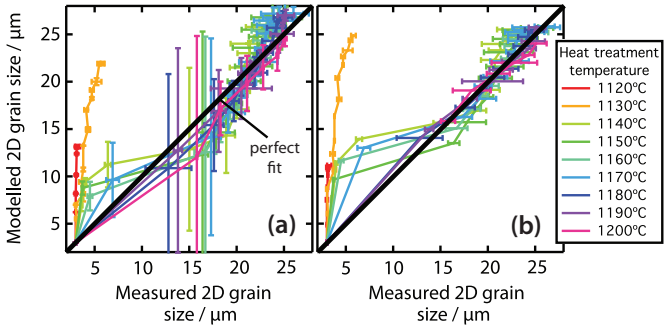

Figure 4: The modelled grain growth sizes using (a) $\bar{D}_{\lim}/k$ values determined from experimental measurements of primary γ', and (b) with $\bar{D}_{\lim}/k$ values determined from Precipicalc predictions of primary γ', are compared to experimentally measured grain sizes.

ential scanning calorimetry (DSC) measurement, predicting the onset of primary γ' dissolution at 1145°C at a constant heating rate [7]). Thermal exposures at 1150°C, 1160°C and 1170°C all showed rapid grain growth as the γ' volume fraction reduces to zero. These isothermal exposures once again appeared to reach a limiting grain size of approximately 25 µm. As expected, at 1180°C, 1190°C and 1200°C, the grain growth rate is further increased, which can be attributed to both the fast dissolution of primary γ', and the temperature dependent thermal activation of grain boundary migration. Once again, these thermal exposures appeared limited by carbides, with grains not growing beyond 25 µm. It therefore appears from this evidence that the r/ϕ value associated with the carbides remains approximately constant for the test durations and temperature ranges examined during this investigation, consistent with the invariability of the MC-carbides observed from the microstructural observations and confirmed by the thermodynamic equilibrium calculations.

4.4. Transient Heat Treatments

Following the forging process of a turbine disc, the time taken for the component to heat up to the desired heat treatment temperature may be significant, and therefore understanding the grain growth response to a transient thermal cycle is valuable, particularly when conducting supersolvus heat treatments.

The mean grain size and volume fraction measurements obtained from the transient heat treatments are shown in Figure 5 (a) and Figure 7 (a) respectively. As temperature increases, the volume fraction of primary γ' can be seen to drop, regardless of the starting temperature. Between 1090°C and 1130°C, the mean grain size appears unaffected by the increased temperature and associated drop in volume fraction. Grain growth begins only once the temperature reaches 1140°C, for material with a starting temperature of 1038°C. From this starting temperature, the mean grain size increases rapidly to 17 µm once 1150°C is reached. An initial acceleration of grain growth is quickly followed by a slower growth rate as the pinning effect from carbides becomes increasingly influential. Unlike the isothermal heat treatments, where the grain growth rate was observed to accelerate between 1150°C and 1200°C, a slowly increasing rate of grain growth is observed. This may simply be attributed to the increased thermal energy available to the migrating grain boundaries. For the heat treatments starting at 1052°C and 1066°C, a similar trend is observed, though the rapid burst of grain growth lags behind the observed mean grain sizes in the samples started at 1038°C. The lower starting temperature is clearly a contributor to grain growth, where the time at elevated temperatures must be critical. It would be expected that the samples having started at a lower temperature, and thus having a longer heat treatment, will result in lower volume fractions of primary γ' at the corresponding interrupted temperatures. However, it is not possible to unequivocally conclude that any difference in grain growth between the starting temperatures is solely dependent on the differences in the γ' volume fraction that as a result of an extended time at elevated temperature beyond experimental error.

5. Modelling

To successfully simulate the grain grain behaviour in nickel-base superalloys, one must account for the temporal γ' precipitate behaviour and its time dependant pinning effect on the migrating γ grain boundaries. The following section describes firstly the prediction of γ' PSDs, and secondly, a grain growth model which incorporates the modelled γ' PSD predictions.

5.1. Simulation of γ' Precipitation

The modelling software *PrecipiCalc* is capable of simultaneous prediction of precipitate nucleation, growth and coarsening. It is based on the Kampmann-Wagner (KW) [34] solution to the well-known Langer and Schwartz (LS) [35] algorithm, describing nucleation and growth of precipitates in a near-critical, metastable liquid and has been calibrated for different alloy systems including RR1000 [36]. For a detailed discussion of the modelling strategy and kinetic equations used, the reader is referred to [37], and for limitations and applications to RR1000 [7]. To assess the extent to which this software could predict the microstructural changes associated with the heat treatments investigated in this study, simulations were run with *PrecipiCalc* using data on the initial microstructure determined experimentally.

In Figure 6 (c) & (d), the primary γ' volume fractions and $\bar{D}_{\lim}/k$ values calculated with *PrecipiCalc* for the isothermal heat treatments are shown. The predictions made at 1120°C and 1130°C show a steady increase in $\bar{D}_{\lim}/k$, as the limiting grain size increases, as function of heat treatment time, with a concomitant decrease in the primary γ' volume fraction. However, the $\bar{D}_{\lim}/k$ values become extremely large with longer time at higher temperatures as the dissolution rate has been overestimated by the model. The predictions for 1140°C and above show complete dissolution, which is expected as the γ' solvus temperature is approximately 1149°C [3]. In general, the predicted trends in $\bar{D}_{\lim}/k$ are in good agreement with the experimental data, i.e. suggesting slow and steady growth at low temperatures, and rapid growth at high temperatures, although there is some disparity between the absolute values. A number of serrations can be observed in the 1150°C isothermal thermal cycle. Close to the γ' solvus temperature, the *PrecipiCalc* model predicts small fluctuations in dissolution and reprecipitation of γ'. These serrations are believed to be artefacts of the

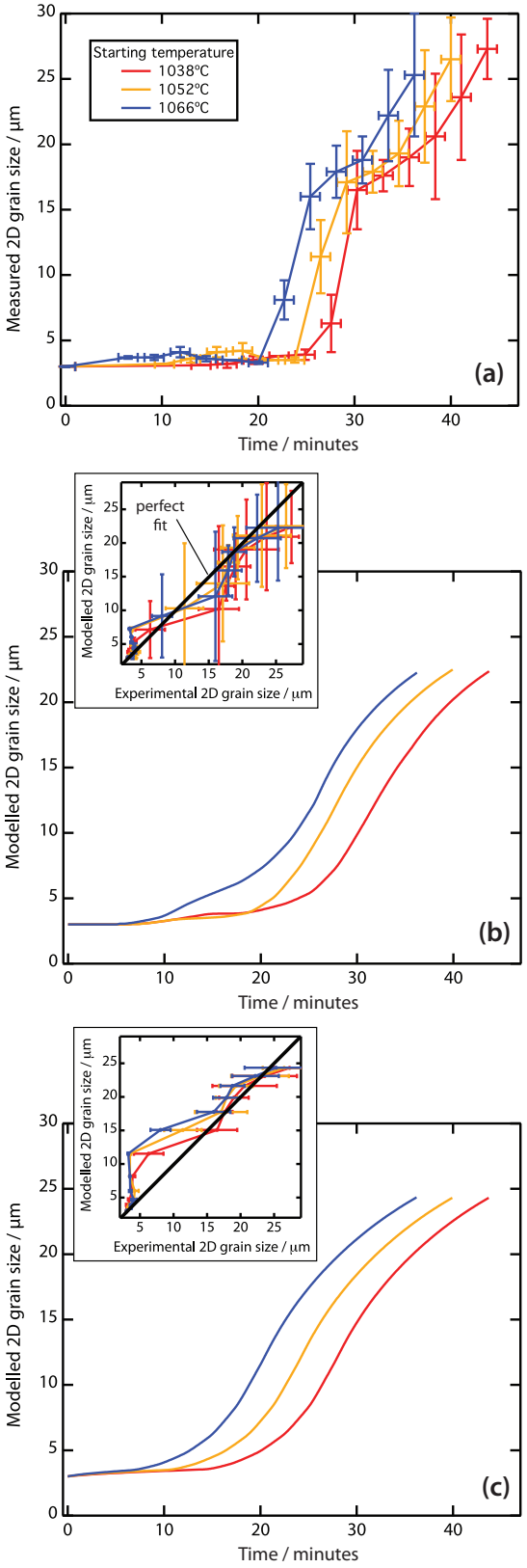

Figure 5: Grain size as a function of time for transient thermal cycles from different starting temperatures. (a) Experimental observations of transient heat treatments. Modelled grain growth results are fitted simultaneously using (b) $\bar{D}_{\mathrm{lim}}/k$ values from measurements, and (c) $\bar{D}_{\mathrm{lim}}/k$ values calculated from *PrecipiCalc* simulations. The modelled 2D grain sizes versus the experimental grain sizes are also shown with each modelled example in the inset graphs.

simulation and are not observed in the experimental observations within experimental error.

The primary γ' volume fractions and $\bar{D}_{\mathrm{lim}}/k$ values predicted using *PrecipiCalc* for the transient thermal exposures are shown in Figure 7 (c) & (d). These data appear to be in good agreement with the values obtained from the transient heat treatments in Figure 5 (a). With the isothermal heat treatments, dissolution of γ' above the solvus temperature is rapid, and hence describing this transformation is difficult at interrupted time intervals. The slower dissolution rate of primary γ' observed with the transient thermal exposures enables $\bar{D}_{\mathrm{lim}}/k$ values to be obtained with greater confidence from experimental measurements, and are found to be well reproduced by the *PrecipiCalc* simulations. The precipitation simulations show an initial increase in volume fraction, with an associated drop in the $\bar{D}_{\mathrm{lim}}/k$ value at 10 minutes, or before (depending upon the starting temperature). However, the time resolution of the experimental measurements was not small enough to ascertain whether this subtle effect is seen in reality.

5.2. Simulation of Grain Growth Behaviour

For the application of the Andersen grain growth model to a microstructurally complex system, such as a polycrystalline nickel-base superalloy, it is necessary for the model to be appropriately modified. The Andersen model considers only the pinning effect of a single distribution of particles, where only the mean radius of the particle distribution is considered. Improvements can therefore be made by considering the effect of the whole size distribution, rather than a mean size alone. Differences between the r/ϕ estimations can be attributed to the high polydispersity of γ' distributions present in nickel-base superalloys, and how the standard deviation of the distribution changes with time. Calculations using a mean distribution radius may therefore produce a biased Zener pinning constant, k, when estimating $\bar{D}_{\mathrm{lim}}$. In the following modification, $\bar{D}_{\mathrm{lim}}$ is calculated by considering multiple histogram bins. Firstly, following Equation 10 for the primary γ' distribution;

$$\bar{D}_{\mathrm{lim}} = k\frac{r_{\gamma'}}{\phi_{\gamma'}} \tag{12}$$

where $r_{\gamma'}$ is the mean distribution radius for the primary γ' precipitates and $\phi_{\gamma'}$ is the volume fraction of the primary γ' distribution. Each histogram bin has a measured frequency for a radius range, between a lower radius, r_{i_1}, and an upper radius, r_{i_2}. For each class, i, the average radius, $\bar{r}_i$ is given simply as

$$\bar{r}_i = \frac{1}{2}(r_{i_1} + r_{i_2}) \tag{13}$$

Assuming the precipitates are spheres, for each histogram bin the precipitate volume is, $V_i = \frac{4}{3}\pi\bar{r}_i^3$. A scaling parameter, α, is defined to normalise each histogram bin against the distribution volume fraction, ϕ, such that

$$\alpha = \frac{1}{\phi}\sum_{i=1}^{N} V_i f_i \tag{14}$$

where N is the maximum histogram bin number and f_i is the measured frequency for the i^{th} bin. Each histogram bin can now be defined in terms of its contribution to the volume fraction, denoted as ϕ_i

$$\phi_i = \frac{V_i f_i}{\alpha} \tag{15}$$

As $\sum_{i=1}^{N} \phi_i = \phi$, the scaling factor can be eliminated by combining Equations 14 and 15, giving

$$\phi_i = \frac{V_i f_i \phi}{\sum_{i=1}^{N} V_i f_i} \tag{16}$$

Each bin in the particle size distribution contributes a proportion of the overall pinning. The value of $\bar{D}_{\text{lim}}$ (applied to any distribution) can now be better described by;

$$\bar{D}_{\text{lim}} = k \left[\sum_{i=1}^{N} \frac{\phi_i}{\bar{r}_i} \right]^{-1} \tag{17}$$

A similar treatment of a size distribution of precipitates on the drag pressure has been investigated by Eivani *et al.* [38]. In that study, the significance of a varying distribution polydispersity to the consequent pinning effect was noted. For this reason, the whole distribution was considered in this study.

As a crude estimate, the $\bar{D}_{\text{lim}}/k$ values should provide a good indicator of grain growth behaviour. The $\bar{D}_{\text{lim}}/k$ values calculated from the isothermal heat treatments measurements are shown in Figure 6 (b). Similarly, in Figure 7 (b), the equivalent calculation for the transient heat treatment measurements are presented. Assuming the pinning effect can be adequately described by the $\bar{D}_{\text{lim}}/k$ values, these can be compared to the grain sizes obtained experimentally. As a general observation, the $\bar{D}_{\text{lim}}/k$ values accounting for the whole γ' distribution predict higher values than the calculations incorporating mean precipitate sizes only. Typically, considering the whole distribution a $\bar{D}_{\text{lim}}/k$ value 30-40% larger is obtained than considering only the mean precipitate size. This difference demonstrates precipitates with sizes deviating from the mean may contribute significantly to the pinning effect and should therefore not be neglected.

The Andersen & Grong [1] grain growth model enables a mean grain size to be predicted for any thermal cycle, as a function of the heat treatment time. From the results obtained in the preceding section, the values obtained for $\bar{D}_{\text{lim}}$ appear highly dependent on the $\bar{D}_{\text{lim}}/k$ quantity. The Andersen & Grong model can therefore be modified to account for the polydispersivity of the γ' distribution through the use of the modified $\bar{D}_{\text{lim}}$ described by Equation 17.

In addition, above the γ' solvus temperature, the γ grains appear to be pinned by carbides, and as such, the expression used to describe grain boundary migration should also account for the contributions from both the primary γ' distribution and the carbide distribution. Limiting grain sizes for both primary γ' pinning and carbide pinning can be described as

$$\bar{D}_{\text{lim}_1} = k_1 \left[\sum_{i=1}^{N} \frac{\phi_i^{\gamma'}}{r_i^{\gamma'}} \right]^{-1} \tag{18}$$

and

$$\bar{D}_{\text{lim}_2} = k_2 \left[\sum_{i=1}^{N} \frac{\phi_i^{\text{carbide}}}{r_i^{\text{carbide}}} \right]^{-1} \tag{19}$$

where $\bar{D}_{\text{lim}_1}$ and $\bar{D}_{\text{lim}_2}$ are the grain size limits with pinning by primary γ' and carbides respectively. The Zener pinning coefficients are assumed to be independent for γ' & carbides and are denoted as k_1, and k_2 respectively. The volume fraction and precipitate radii of the i^{th} bin within the distribution are denoted as $\phi_i^{\gamma'}$ & $r_i^{\gamma'}$ for γ' and ϕ_i^{carbide} & r_i^{carbide} for the carbide distribution. From microscopy observations, the carbides are not observed to decorate the grain boundaries when the primary γ' remains present, and therefore do not contribute to the pinning effect until all of the γ' is dissolved. Instead of simply adding the terms $1/\bar{D}_{\text{lim}_1}$ and $1/\bar{D}_{\text{lim}_2}$ in series, each is raised by the power, m, followed by the m^{th} root taken of the sum of the two pinning contributions. For the calculations conducted in this study, m was arbitrarily taken to be 5, which is a sufficiently large number to enable γ' to dominate when present, and the carbides to dominate once the γ' has dissolved. The fits were seen to be insensitive to the value of m selected for $m \geq 5$.

Pinning by secondary and tertiary γ' may also be dismissed. DSC analysis has previously revealed that complete dissolution of secondary and tertiary γ' occurs once temperatures of 1115°C and 1000°C respectively had been reached [7]. Therefore, at the solution heat treatment temperatures considered in this study, these precipitate distributions would have either entirely dissolved, or will be present only in very small volume fractions. It is hence assumed that the pinning contribution of intragranular γ' is negligible. Accounting for the appropriate RR1000 specific pinning contributions, the Andersen & Grong model now takes the following form;

$$\int_{D_0}^{\bar{D}_t} \frac{\mathrm{d}\bar{D}}{\left[\frac{1}{\bar{D}} - \left[\left(\frac{1}{\bar{D}_{\text{lim}_1}} \right)^m + \left(\frac{1}{\bar{D}_{\text{lim}_2}} \right)^m \right]^{\frac{1}{m}} \right]^{\frac{1}{n}-1}} = I = \int_{t_1}^{t_2} M_0^* \exp\left(\frac{-Q_{\text{app}}}{RT} \right) \mathrm{d}t \tag{20}$$

Equation 20 may be solved by various methods. Firstly, the derivative of the grain growth function (in the format of Equation 9) could be fitted to the experimental data. This is possible when the derivative of the experimental data can be reliably obtained. In practice, this is very simple to obtain, although its accuracy is largely dependent on the number of experimental data points and the degree of scatter. This may be aided by parameterising the data, though this approach once again relies upon a large number of data points for confidence. To help the fitting of the data, a smoothing algorithm could also be used. Following smoothing, the experimental data may then be visually inspected to ensure this process had not lost information to describe the trends in the grain growth response.

In this study, the integral in Equation 20 was evaluated numerically, with the experimental times used to calculate the

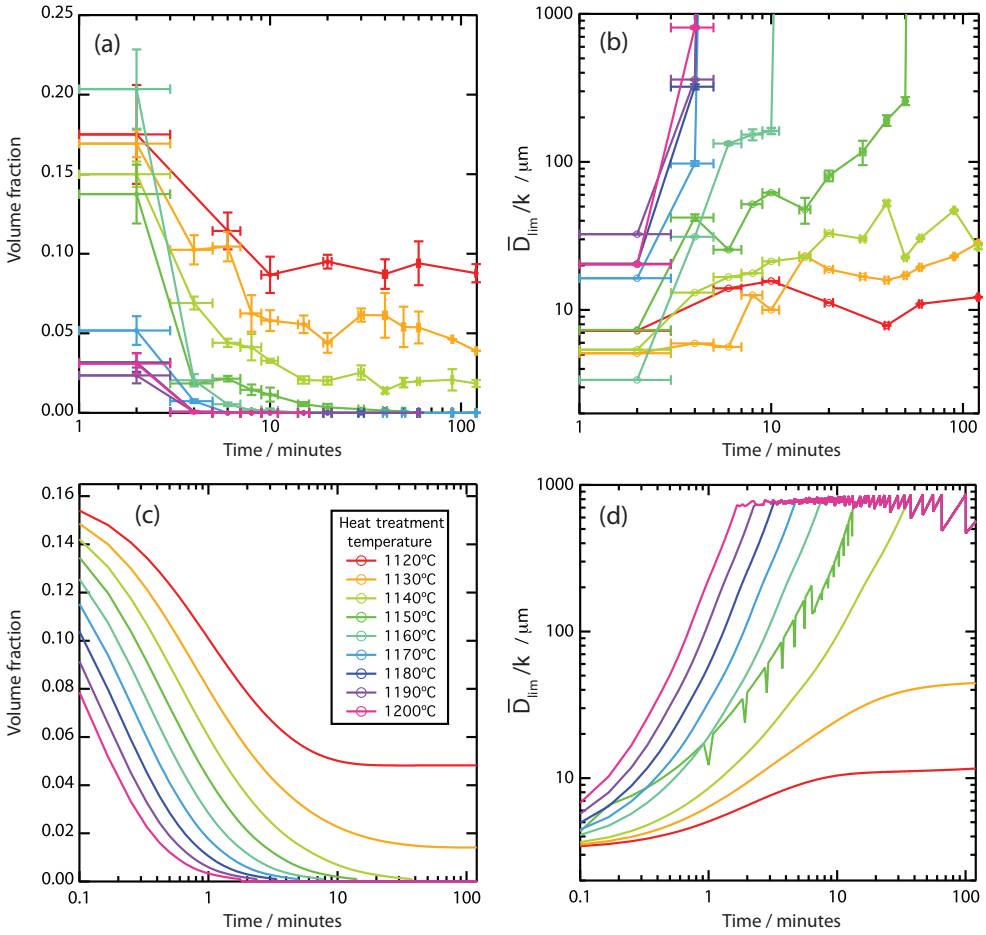

Figure 6: Volume fraction and calculated $\bar{D}_{\text{lim}}/k$ values for isothermal exposures; (a) & (b) from measurements, and (c) & (d) from *PrecipiCalc* simulations, respectively. These data can be used to approximate the limiting grain size for each thermal cycle, at any corresponding time.

mean grain size, $\bar{D}_t$. The integral was solved at 500 interpolated increments between each value of t. Where $t = 0$, $\bar{D}_0 = 4.5\,\mu\text{m}$ (from a 2D experimental measurement of 3.0 µm) was used. The left hand side integral of Equation 20 was evaluated using Simpsons' rule. After an initial guess for $\bar{D}_t$, convergence of this value was found using the bisection method for each time step, t, re-evaluating the LHS integral with each iteration until this was approximately equal to the RHS integral.

The function could then be fitted directly to the experimentally measured values of $\bar{D}$ by varying, Q_{app}, k_1, k_2, n and M_0^*. For each time step solved, the corresponding $\bar{D}_{\text{lim}_1}$ value was used. These were either experimentally determined or calculated from *PrecipiCalc* predictions. Microscopy observations show the carbides did not appear to change as a function of time or temperature, giving a fixed value of $\bar{D}_{\text{lim}}/k$ throughout the simulations. Using the measured carbide distribution, the $\bar{D}_{\text{lim}_2} = \sum_{i=1}^{N} r_i/\phi_i$ value was fixed at 49.2 µm, where $k_2 \times 49.2$ represents the greatest 3D mean grain size (in microns) for this material. In summary, the model input consists of grain size measurements, $\bar{D}$, the associated $\bar{D}_{\text{lim}_1}$, $\bar{D}_{\text{lim}_2}$, and temperature.

For each time step solved, a fitting index, i, was assigned along with a corresponding fitting score, δ_i. A linear weighting was used, based upon the following expression:

$$\delta_i = \frac{I_i^{\text{calculated}}}{I_i^{\text{target}}} \tag{21}$$

hence, when $\delta_i = 1$, a perfect fit is obtained. The values of I_i^{target} were calculated by solving the RHS integral of Equation 20 and $I_i^{\text{calculated}}$ was calculated from the LHS integral of Equation 20 using iterative guesses of $\bar{D}_t$. A fitting index for all time steps was then calculated by

$$\delta = \sum_{i=1}^{N} |\delta_i| \tag{22}$$

The above expression was calculated during each iteration of a fitting procedure in which all the data obtained following the various isothermal or transient heat treatments were fitted simultaneously. This enabled the global minimum of all data to be found at the corresponding minimum value of δ. The best fit was obtained by simultaneously changing each variable using a specially developed searching algorithm.

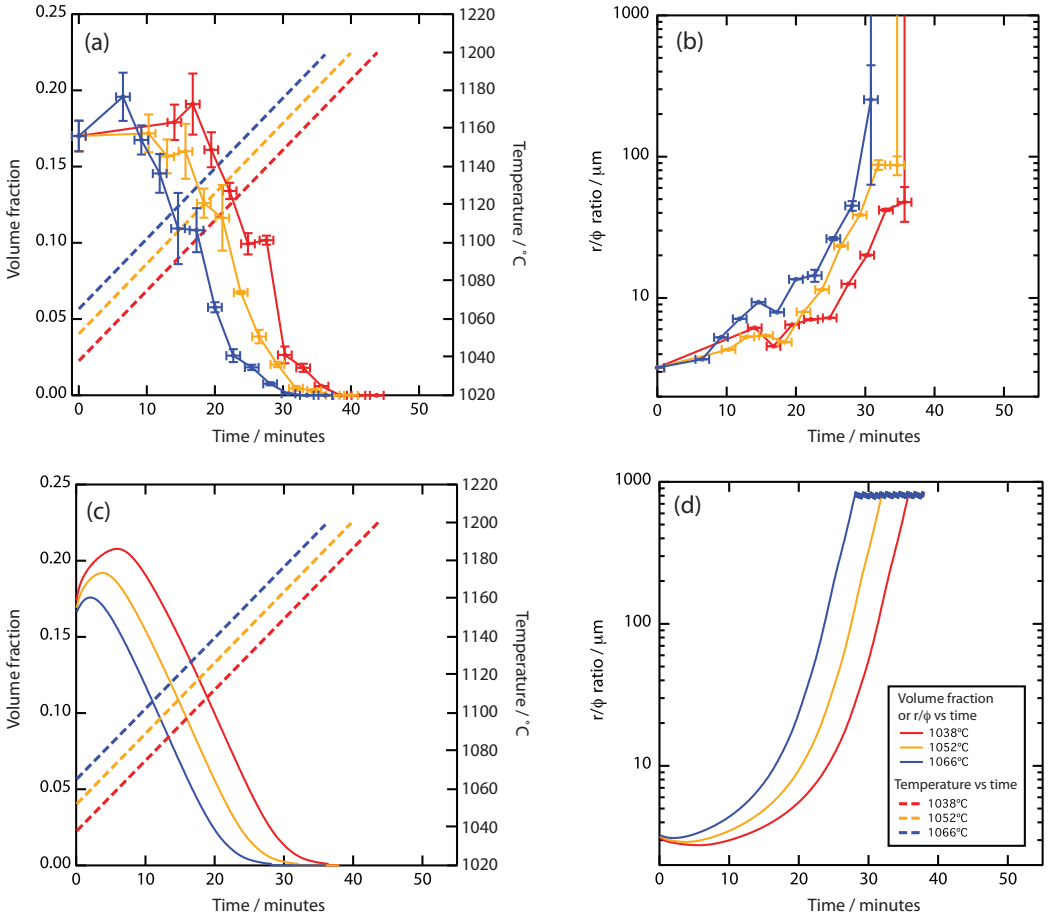

Figure 7: Volume fractions and calculated $\bar{D}_{\mathrm{lim}}/k$ values for the transient heat treatments. (a) and (b) are from measurements, and (c) and (d) are derived from predictions made using *PrecipiCalc*. For reference, the temperature is also plotted with respect to time with the volume fraction data.

5.3. Grain Growth Model Results and Discussion

The model predictions of the grain growth that occurs during the isothermal heat treatments are shown in Figure 3 (b) and (c), where the $\bar{D}_{\mathrm{lim}}/k$ values shown in (b) were obtained by fitting all of the experimental data simultaneously, whilst the $\bar{D}_{\mathrm{lim}}/k$ values shown in (c) were obtained by fitting to the results obtained from *PrecipiCalc* simulations. These results have been converted from 3D to 2D grain sizes for direct comparison against the experimental measurements. A summary of the fitting coefficients obtained for all plotted simulations are shown in Table 1.

In Figure 4, the success of fitting the isothermal heat treatments is shown by plotting the modelled 2D grain sizes versus the experimental 2D grain sizes. Figure 4 (a) corresponds to data fitted using $\bar{D}_{\mathrm{lim}}/k$ values from experimental measurements and Figure 4 (b) corresponds to $\bar{D}_{\mathrm{lim}}/k$ values determined from *PrecipiCalc* simulations. Errors have been plotted for experimental measurements and for modelling results which used experimental input data for $\bar{D}_{\mathrm{lim}}/k$ values. This was not possible when using *PrecipiCalc* data as uncertainties are not generated from precipitation predictions. It can be seen from Figure 3 (b) and Figure 4 (a) that fitting all of the isothermal experimental data simultaneously provides good correlation to the experimental data, particularly for temperatures 1140°C and above. However, the modelled grain sizes for the heat treatments at 1120°C and 1130°C were underestimated. At these temperatures, the grain growth behaviour is heavily restricted by the presence of pinning primary γ', and experimentally, little growth was observed. As the measured $\bar{D}_{\mathrm{lim}_i}$ increases, the model predicts significantly more grain growth than is observed experimentally. The sudden growth rate change observed experimentally between 1130°C and 1140°C indicates the behaviour is very sensitive to temperature. Clearly, small experimental discrepancies in the temperature or precipitate measurements could account for some of this error, though it is unlikely fully explain the difference. If a single $\bar{D}_{\mathrm{lim}_i}$ value is overestimated, the grain size for the corresponding time interval would be permitted to increase. As grain size is only predicted to increase or remain constant, this error would not be corrected during the modelling of consequent time steps. Therefore, experimental scatter may significantly influence the predicted behaviour. This issue does not arise with the $\bar{D}_{\mathrm{lim}}/k$ calculated from the *PrecipiCalc* predictions, due to the absence of scatter from these data.

In Figure 3 (c) and Figure 4 (b), the grain growth modelling predictions are shown using the $\bar{D}_{\mathrm{lim}}/k$ values calculated from *PrecipiCalc*. These results were able to better reproduce the

isothermal experimental data. For the 1120°C isothermal heat treatment, some grain growth is predicted, though is more restricted than than using $\bar{D}_{\lim}/k$ values obtained from the experimental measurements. Above 1120°C, *PrecipiCalc* predicts the $\bar{D}_{\lim}/k$ reduces significantly (see Figure 6 (d)), and consequently grain growth above this temperature is accelerated. A previous study by Collins *et al.* [7] has shown *PrecipiCalc* underestimates the primary γ' solvus temperature of RR1000, which directly accounts for the grain growth model discrepancy observed in this study. The influence of scatter in $\bar{D}_{\lim}/k$ values suggests that modelling the behaviour of pinning precipitates is beneficial, though will be limited by the accuracy of dissolution temperatures. Furthermore, as *PrecipiCalc* is only capable of a 1-D prediction of precipitation behaviour it does not account for the precipitate spacing, and can therefore not be used to asses the influence of this factor on the grain growth behaviour. Only by accounting for this, can the individual fitting coefficients be further scrutinised to eliminate other influencing factors, such as temperature dependence.

The maximum grain sizes, limited by the carbide $\bar{D}_{\lim_2}$ value, were shown to be in good agreement with experimental observations. For the carbide distribution, where $\bar{D}_{\lim_2}$ was fixed at 49.2 μm, assuming $k_2 = 0.835$, for example, and converting to 2D, the mean grain size expected from a linear intercept method is therefore 27.4 μm. This compares favourably with the maximum grain size observed in the isothermal heat treatments, as shown by Figure 3 (a). Using Equation 10, where k is assumed to be the Zener constant, 4/3, $\phi = 0.0022$ and $\bar{r} = 70$ nm, a maximum 2D grain size of 28.3 μm is obtained, which slightly overestimates the maximum grain size observed for isothermal heat treatments. Furthermore, the value, k_2 is quite different from the Zener constant as the full particle size distribution has been accounted for. Therefore, the value of k_2, or indeed k_1, may be thought of as a size distribution dependent grain size limit constant.

It is accepted that although carbides other than MC are thermodynamically stable at lower temperatures, their occurrence is kinetically inhibited. Hence, the volume fraction of any such species will be small. Among such phases, the $M_{23}C_6$ is formed by the decomposition of MC (via $MC + \gamma \rightarrow M_{23}C_6 + \gamma'$ [39]), though this occurs at lower service-type temperatures (~750°C [6]).

In this study, this distribution have been classified as carbides, this may include some oxy-carbides of a similar size. Any smaller scale particles, such as nm-scale HfO_2 particles, have not been measured in this study. Importantly, no evidence of grain boundary pinning by other phases, such as topologically close packed (TCP) phases or borides was observed, nor with annealing twins. Neglecting oxy-carbides may explain why the value of k_2 has been predicted to be lower than k_1.

The modelling results of the transient thermal exposures are shown in Figure 5 (b) and (c). In (b), the $\bar{D}_{\lim}/k$ values from the experimental measurements have been used, fitting all measurements from both transient and isothermal heat treatments simultaneously. In (c), the $\bar{D}_{\lim}/k$ values were obtained from the *PrecipiCalc* simulations, again fitting all (isothermal and transient) data simultaneously. The fitting coefficients obtained for the transient heat treatments are summarised in Table 1. The

Table 1: Fitting coefficients for the isothermal heat treatments using $\bar{D}_{\lim}/k$ values determined from (a) experimental measurements and (b) *PrecipiCalc* simulations. Both isothermal and transient heat treatment data sets are fitted together, again using $\bar{D}_{\lim}/k$ values from (c) experimental measurements and (d) *PrecipiCalc* simulations.

Fitted data set	M_0^* ($m^2 s^{-1}$)	k_1	k_2	Q_{app} (kJ mol^{-1})	n
(a)	0.515	1.78	0.835	334	0.465
(b)	0.415	1.47	0.791	342	0.444
(c)	0.845	1.10	0.801	341	0.463
(d)	0.330	1.52	0.878	338	0.448

scatter in the experimentally measured $\bar{D}_{\lim}/k$ values give rise to different initial growth rates dependent on the starting temperatures, which is not observed for $\bar{D}_{\lim}/k$ values calculated from the *PrecipiCalc* simulations. Again, the rate of dissolution for the *PrecipiCalc* is too rapid, which explains the onset of grain growth at an earlier time than is observed experientially.

Attempts were made to fit the transient heat treatments simultaneously, without including the isothermal heat treatments. This resulted in unreliable fitting of the grain growth coefficients, being most significant for the value of k_2. As the transient heat treatments are not experimentally observed to reach a maximum grain size, the model becomes unreliable without confidently determining a $\bar{D}_{\lim_2}$ value. Using both the isothermal and transient heat treatment data together eliminates this problem. This observation indicates that when an additional coefficient is introduced, the experimental data must describe the behaviour unique to this parameter, ensuring reliable fitting.

As a comparison with other metallurgical systems that have used the Andersen & Grong model, the mobility constant, M_0^* for microalloyed-Nb steel, microalloyed-Ti and austenitic steel were 7.7×10^{-3} m^2 s^{-1} [1], 3.7×10^{-3} m^2 s^{-1} [1], and 4.1×10^{-3} m^2 s^{-1} [23] respectively. In these examples, Equation 11 was evaluated assuming $n = 0.5$. However, Andersen demonstrated that the grain growth model is highly sensitive to the coefficient, and with values typical of this study of $n \simeq 0.45$, the grain growth rate is significantly lower than when $n = 0.5$. Fixing the highest permissible value of n will therefore overestimate the rate of growth, and hence when fitting, will be compensated by lowering the value M_0^*. A value of $n \simeq 0.5$ is true only for a pure material, and hence, it is unsuitable to assume this value for a highly alloyed material. Furthermore, the treatment of $\bar{D}_{\lim}$ in this study to account for a full particle size distribution will require a higher value of M_0^* than if a mean particle size alone was used to calculate $\bar{D}_{\lim}$. The apparent grain boundary activation energy values of ~220 kJ mol^{-1} for microalloyed steel [1] or 291 kJ mol^{-1} used by Seetharaman *et al.* [22] for a gamma-titanium alloy indicates the value of ~340 kJ mol^{-1} found in this study is reasonable for an engineering alloy.

Referring to the grain growth coefficients obtained from the fitting of each data set in Table 1, the values appear similar irrespective of the type of data being fitted. Notably n, Q_{app} and k_2 show very high agreement. The largest disagreement of M_0^* and k_1 occurs when fitting data with $\bar{D}_{\lim}/k$ data from measure-

ments. This may be expected as data fitting was found to be very sensitive to scatter in the $\bar{D}_{\lim}/k$ values. Significant disagreement is not observed with input data used from *PrecipiCalc* simulations. In this case, the value of k_1 of ~ 1.5 is closer to the classical value of 4/3 predicted by Zener. As stated before, this value is expected to differ in the present study due to the model accounting for the whole precipitate size distribution, rather than a mean size alone.

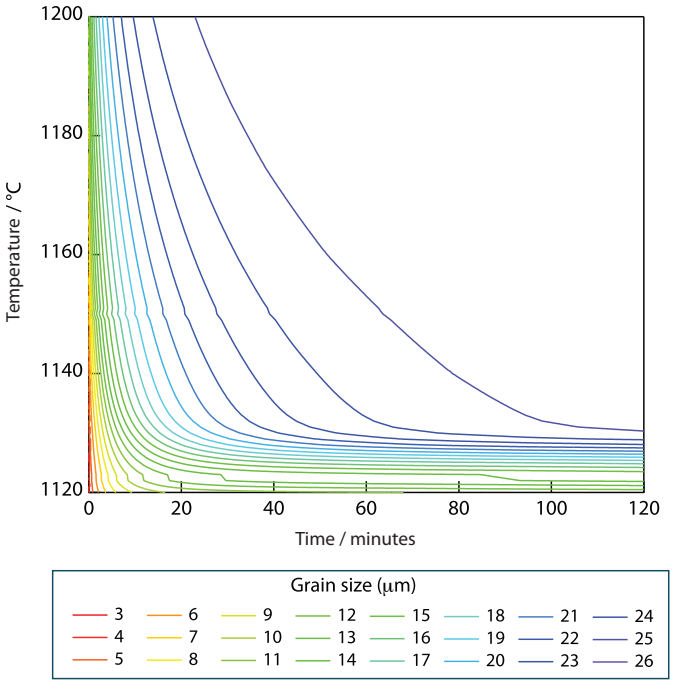

Figure 8: Predicted time-temperature-transformation graph of grain sizes using primary γ' data predicted by *PrecipiCalc*, between 0 & 20 minutes and 20 & 120 minutes in (a) and (b), respectively.

The ultimate application of the grain growth measurements and predictions obtained during this study is to aid the selection of suitable heat treatments during a DMHT manufacturing process. The fitting strategy employed has enabled grain growth coefficients to be obtained, thus describing the behaviour of RR1000 during near-solvus heat treatments. Using this calibrated data, Equation 20 can be re-solved for grain size, $\bar{D}$, for any desired time, t. Simulated $\bar{D}_{\lim}/k$ data was then obtained from *PrecipiCalc* at temperatures between 1120°C and 1200°C in 1°C increments, for times up to 2 hours in 5 second steps. This enabled a grain size, $\bar{D}$, to be obtained for each corresponding $\bar{D}_{\lim}/k$ and t. In the example shown here, values of the necessary coefficients from the isothermal thermal exposures with *PrecipiCalc* measurements (Table 1) were used, enabling the right hand side of Equation 20 to be recalculated.

The modelled grain sizes with respect to time and temperature are presented as a contour plot in Figure 8, which may also be considered a time-temperature-transformation (TTT) representation. Grain sizes have been converted to 2D linear intercept measurements. Any time and temperature can subsequently be selected, providing a mean 2D grain size prediction. As *PrecipiCalc* allows the input of any arbitrary thermal cycle, as does the Andersen & Grong [1] model, similar grain size predictions could be obtained for any complex processing heat treatment. It has therefore been shown that a series of grain size measurements alone, ensuring they cover a suitable time and temperature range, enables high resolution prediction of grain size; a capability highly desirable for components subjected to location specific heat treatments.

5.4. Summary

In this study, the grain growth behaviour of the polycrystalline nickel-base superalloy, RR1000, has been investigated. Isothermal and transient heat treatments have been carried out in the vicinity of the primary γ' solvus temperature, to understand the relationship between the pinning primary γ' and the grain growth behaviour. Microscopy revealed the presence of MC carbides that impede grain boundary migration above the γ' solvus temperature, further limiting grain growth. Volume fraction and precipitate sizes were measured, providing predicted values of $\bar{D}_{\lim}$ for each heat treatment assessed. The grain growth behaviour was subsequently modelled using an adapted version of the model proposed by Andersen & Grong [1], accounting for the presence of carbides, and the inclusion of whole primary γ' PSD. In this way the grain behaviour could be approximated by 5 independent parameters. All of the parameters can be fitted using the grain growth data alone, without requiring any of these parameters to be obtained from other experiments. The results obtained with such models were seen to be sensitive to the accuracy with which the parameter, $\bar{D}_{\lim}/k$ could be determined. By using *PrecipiCalc* to simulate the dissolution of primary γ', smooth $\bar{D}_{\lim}/k$ values were obtained, thereby providing superior fitting results, and thus fitting coefficients. Using these fitting coefficients, a high resolution TTT plot of grain size with respect to time and temperature was produced, with sufficient detail for the application to component manufacture with location specific heat treatments, such as DMHT.

Acknowledgments

The authors would like to acknowledge and thank the EPSRC and Rolls-Royce plc. for their financial support. HJS & BDC were supported by the EPSRC/Rolls-Royce Strategic Partnership (EP/H500375/1) and DMC by an EPSRC studentship. Thanks are extended to J.R. May for assistance during metallographic preparation and J.W. Aveson for useful discussions.

References

[1] Andersen, I., Grong, Ø.. Acta Metall Mater 1995;43:2673.

[2] Sims, C., Stoloff, N., Hagel, W., editors. Superalloys II- High Temperature Materials for Aerospace and Industrial Power. John Wiley & Sons, Inc; 1987.

[3] Connor, L.. The Development of a Dual Microstructure Heat Treated Ni-base Superalloy for Turbine Disc Applications. Ph.D. thesis; University of Cambridge; 2009.

[4] Jackson, M., Reed, R.. Mater Sci Eng A 1999;259:85.

[5] Kozar, R., Suzuki, A., Milligan, W., Schirra, J., Savage, M., Pollock, T.. Metall Mater Trans A 2009;40:1588.

[6] Reed, R.. The Superalloys - Fundamentals and Applications. Cambridge, UK: Cambridge University Press; 2006.

[7] Collins, D., Stone, H.. A modelling approach to heat treatment optimisation in a nickel-base superalloy. Submitted to Mater Sci Eng A 2013;.

[8] Williams, J., Jr., E.S.. Acta Mater 2003;51:5775.

[9] Mourer, D., Williams, J.. In: Green, K., Pollock, T., Harada, H., Howson, T., Reed, R., Schirra, J., et al., editors. Superalloys 2004. TMS (The Minerals, Metals & Materials Society); 2004, p. 401–407.

[10] Hyzak, J., Macintyre, C., Sundberg, D.. In: Reichman, S., Duhl, D., Maurer, G., Antolovich, S., Lund, C., editors. Superalloys 1988. The Metallurgical Society; 1988, p. 121–130.

[11] Mitchell, R., Lempsky, J., Ramanathan, R., Li, H., Perkins, K., Connor, L.. In: Reed, R., Green, K., Caron, P., Gabb, T., Fahrmann, M., Huron, E., et al., editors. Superalloys 2008. TMS (The Minerals, Metals & Materials Society); 2008, p. 347–356.

[12] Hessel, J., Voice, W., James, A., Blackham, S., Small, C., Winstone, M.. Nickel alloy for turbine engine component. Patent Number EP0803585; 2000.

[13] Porter, D., Easterling, K.. Phase Transformations in Metals and Alloys. CRC Press; second ed.; 1992.

[14] Hu, H., Rath, B.. Metall Mater Trans B 1970;1:3181.

[15] Higgins, G., Wiryolukito, S., Nash, P.. Mater Sci Forum 1992;94-96:671.

[16] Zener, C.. (Quoted by CS Smith) Trans Am Inst Min Metall Pet Eng 1948;15:15.

[17] Song, K., Aindow, M.. Mater Sci Eng A 2007;479:365.

[18] May, J.. Processing, microstructure and mechanical properties of an advanced nickel base powder metallurgy superalloy. Ph.D. thesis; Swansea University; 2011.

[19] Apel, M., Böttger, B., Rudnizki, J., Schaffnit, P., Steinbach, I.. ISIJ Int 2009;49:1024.

[20] Wang, G., Xu, D., Payton, E., Ma, N., Yang, R., Mills, M., et al. Acta Mater 2011;59:4587.

[21] Andersen, I., Grong, Ø., Ryum, N.. Acta Metall Mater 1995;43:2689.

[22] Seetharaman, V., Semiatin, S.. Metall Mater Trans A 1997;28:947.

[23] Bernhard, C., Reiter, J., Presslinger, H.. Metall Mater Trans B 2008;39:885.

[24] Tsuchiya, S., Ohno, M., Matsuura, K., Isobe, K.. Acta Mater 2011;59:3334.

[25] Manohar, P.A., Ferry, M., Chandra, T.. ISIJ Int 1998;38:913.

[26] Collins, D., Heenan, R., Stone, H.. Metall Mater Trans A 2011;42:49.

[27] ASTM Standard E112-10. Standard Test Methods for Determining Average Grain Size. West Conshohocken, PA: ASTM International; 2010.

[28] Rasband, W.. ImageJ. U.S. National Institute of Health; 1997-2009.

[29] Abramoff, M.. Biophotonics Int 2004;11:36.

[30] Hosford, W.. Physical Metallurgy. Boca Raton, FL: CRC Press; 2005.

[31] JMatPro 6.1 *http://www.sentesoftware.co.uk/*. Sente Software Ltd; 2012.

[32] Hunt, D.. The stability and mechanical properties of a nickel-base superalloy. Ph.D. thesis; University of Cambridge; 2001.

[33] Xu, S., Dickson, J., Koul, A.. Metall Mater Trans A 1998;29:2687.

[34] Kampmann, R., Wagner, R.. Materials Science and Technology: Phase Transformations in Materials; vol. VCH Verlagsgesellschaft mbH. 1991.

[35] Langer, J., Schwartz, A.. Phys Rev A 1980;21:948.

[36] Olsen, G., Jou, H.J., Sebastian, J., Misra, A., Locci, I., Hull, D.. In: Reed, R., Green, K., Caron, P., Gabb, T., Fahrmann, M., Huron, E., et al., editors. Superalloys 2008. TMS (The Minerals, Metals & Materials Society); 2008, p. 923–932.

[37] Jou, H., Voorhees, P., Olsen, G.. In: Green, K., Pollock, T., Harada, H., Howson, T., Reed, R., Schirra, J., et al., editors. Superalloys 2004. The Minerals, Metals & Materials Society; 2004, p. 877–886.

[38] Eivani, A., Valipour, S., Ahmed, H., Zhou, J., Duszczyk, J.. Metall Mater Trans A 2011;42:1109.

[39] Sabol, G.P., Stickler, R.. Phys Status Solidi B 1969;35:11.